Airborne coherent wind lidar measurements of the momentum flux profile from orographically induced gravity waves

Benjamin Witschas[1], Sonja Gisinger[1], Stephan Rahm[1], Andreas Dörnbrack[1], David C. Fritts[2], and Markus Rapp[1]

[1]Deutsches Zentrum für Luft- und Raumfahrt e.V. (DLR), Institut für Physik der Atmosphäre, 82234 Oberpfaffenhofen, Germany
[2]GATS, Boulder, CO, USA

Correspondence: Benjamin Witschas, (Benjamin.Witschas@dlr.de)

Abstract. In the course of the GW-LCYCLE II campaign, conducted in Jan/Feb 2016 from Kiruna, Sweden, coherent Doppler wind lidar (2-μm DWL) measurements were performed from the DLR Falcon aircraft to investigate small-scale gravity waves induced by flow across the Scandinavian Alps. During a mountain wave event on 28 January 2016, a novel momentum flux (MF) scan pattern with fore and aft propagating laser beams was applied to the 2-μm DWL. This allows to measure the vertical wind and the horizontal wind along the flight track simultaneously, and hence, enables to derive the horizontal momentum flux profile. The functionality of this method and the corresponding retrieval algorithm is validated using a comparison against in-situ wind data measured by the High Altitude and Long Range (HALO) aircraft which was also deployed in Kiruna for the POLSTRACC (Polar Stratosphere in a Changing Climate) campaign. Based on that, the systematic and random error of the wind speeds retrieved from the 2-μm DWL observations are determined. Further, the measurements performed on that day are used to reveal significant changes in the horizontal wavelengths of the vertical wind speed and of the leg-averaged momentum fluxes in the tropopause inversion layer (TIL) region, which are induced by interfacial waves.

1 Introduction

Gravity waves (GWs) vertically connect the lower atmosphere, where they are primarily excited by flow over orography, convection, or flow deformation for instance caused by jets and fronts, with the upper atmosphere (Fritts and Alexander, 2003). While propagating, GWs carry momentum and energy and deposit them in regions where they dissipate. Whereas there is a general understanding of processes launching GWs, the nature of wave source spectra is more complex (Chen et al., 2007). Thus, there is still a need for a better characterization of GW sources to properly describe the dynamical coupling of the lower and the upper atmosphere. For this reason, several field campaigns with sophisticated airborne and ground-based instrumentation were performed within the last decades for instance the T-Rex campaign (Grubišić et al., 2008; Smith et al., 2008), the GW-LCYCLE I (Wagner et al., 2017; Ehard et al., 2016a) and GW-LCYCLE II campaign (Gisinger et al., 2020), DEEPWAVE (Fritts et al., 2016) and SOUTHTRAC (Rapp et al., 2020). During a few of these campaigns, it was demonstrated that both ground-based and airborne lidar instruments are valuable for characterizing GW properties, as they provide vertically-resolved information of dynamically relevant quantities for instance wind speed, temperature, and density. With such kind of

measurements, altitudes of ≈ 15 to 100 km are covered (e.g., Fritts et al., 2016; Kaifler et al., 2020; Kaifler and Kaifler, 2021;
25 Kaifler et al., 2021; Rapp et al., 2020).

To gain further knowledge about the excitation region of GWs in the troposphere, DLR's coherent Doppler wind lidar
(2-μm DWL) was deployed on the Falcon aircraft during the GW-LCYCLE I (Gravity Wave Life Cycle) campaign (Dec 2013)
(Wagner et al., 2017; Ehard et al., 2016a) and the GW-LCYCLE II campaign (Jan/Feb 2014), both flown out of Kiruna,
Sweden. During GW-LCYCLE I, the 2-μm DWL measured either horizontal or vertical wind speeds and demonstrated that
30 the horizontal scales of vertical wind and horizontal wind perturbations differ by an order of magnitude and that the spectral
features can be related to the high-frequency (vertical wind) and low-frequency (horizontal wind) part of the topography
spectrum (Witschas et al., 2017). A similar observation was reported by Smith and Kruse (2017) based on airborne in-situ
measurements. Further, Witschas et al. (2017) discussed the advantageousness of measuring the vertical wind speed w and the
horizontal wind speed along flight direction u_{par} simultaneously, as this would allow to additionally quantify the propagation
35 direction of the GWs and the corresponding momentum transport. To do so, a novel momentum flux (MF) scan pattern with
fore and aft propagating laser beams was applied to the 2-μm DWL for the first time during the GW-LCYCLE II campaign.
From that, the leg-averaged momentum flux (MF $= \overline{\rho}\,\overline{u'_{\mathrm{par}}\,w'}$) transported by GWs can be derived (Eliassen and Palm, 1961;
Smith et al., 2016), where the prime indicates the perturbations of the respective quantity, the overline denotes the average
along the flight leg and $\overline{\rho}$ denotes the mean air density.

40 In this paper, the novel MF-scan procedure and the corresponding retrieval algorithms are introduced employing 2-μm DWL
measurements acquired on the flight performed on 28 January 2016 during a mountain wave event. The quality of the de-
rived wind components is estimated using a comparison against in-situ wind data measured by the High Altitude and Long
Range (HALO) aircraft which was flying coordinated with the Falcon aircraft on that day. Based on the 2-μm DWL data,
significant changes in the power spectra of the vertical velocity field and the leg-averaged momentum flux in the tropopause
45 inversion layer (TIL) region are revealed.

This paper is structured as follows. First, an overview of the GW-LCYCLE II campaign is given (Sect. 2), followed by a
short introduction of the 2-μm DWL instrument (Sect. 3) including the description of the instrumental setup (Sect. 3.1), the
measurement principle (Sect. 3.2) as well as the data processing steps (Sect. 3.3). The results of the wind data analyses are
discussed in Sect. 4, followed by a summary given in Sect. 5.

2   The GW-LCYCLE II campaign

50

To investigate the persistence of GWs from their generation in the troposphere through to their dissipation, the GW-LCYCLE II
(Gravity Wave Life Cycle Experiment II) campaign was conducted from 12 January 2016 to 3 February 2016 in Northern
Scandinavia. With that, it extended the data set acquired during the precursor campaign GW-CYCLE I, which took place in
December 2013 (Ehard et al., 2016b; Wagner et al., 2017; Witschas et al., 2017). Northern Scandinavia is a well-suited region
55 to study coupling processes between the troposphere, the stratosphere, and the mesosphere, as the north-south orientation of

the Scandinavian mountain ridge together with westerly blowing winds lead to the excitation of mountain waves that can then propagate upwards, provided that the background winds are favorable (Dörnbrack et al., 2001).

2.1 Instrumentation overview

During GW-LCYCLE II, several ground-based and airborne instruments on different sites were deployed. The CORAL li-
dar (Reichert et al., 2019; Kaifler and Kaifler, 2021), the Advanced Atmospheric Temperature Mapper - AMTM (Pautet et al., 2014) as well as the All-Sky Interferometric Meteor Radar - SKiYMET (Lukianova et al., 2018) were collocated in Sodankylä, Finland (67.4° N, 26.6° E), the Middle Atmosphere Alomar Radar System - MAARSY (Latteck et al., 2012; Stober et al., 2012), a second AMTM and a the Alomar Rayleigh/Mie/Raman lidar system (Baumgarten, 2010) were operated on the west coast of Norway in Alomar (69.3° N, 16.0° E), and a third AMTM, a radiosonde launch-site and the DLR Falcon research
aircraft were situated in Kiruna, Sweden (67.8° N, 20.3° E). Whereas the ground-based instruments were mainly meant for probing the stratosphere and mesosphere, the airborne systems on board the Falcon were used to probe the GW excitation region in the troposphere. Besides an air-glow imager (Wüst et al., 2019) and in-situ instruments used to measure tropospheric and stratospheric trace gases as water vapor concentration, SO_2, CO, N_2O, CH_4 and CO_2, the Falcon was equipped with a downward looking coherent 2-μm DWL that is very useful for characterizing the spectral features of mountain waves by ex-
ploiting measurements of either horizontal or vertical wind speed profiles, respectively (Witschas et al., 2017). In addition to the 2-μm DWL wind data, the horizontal and the vertical wind speed was measured at flight level by the Falcon nose-boom employing a flow angle sensor (Rosemount model 858) together with an inertial reference system (Honeywell Lasernav YG 1779) as described by Bögel and Baumann (1991); Krautstrunk and Giez (2012). Jointly with the Falcon, the HALO aircraft was deployed in Kiruna, Sweden in the same period, aiming to investigate the Polar Stratosphere in a Changing Climate (POL-
STRACC). To do so, HALO was equipped with 10 in-situ and 3 remote sensing instruments measuring the composition of the upper troposphere and the lower stratosphere. A detailed overview of the POLSTRACC campaign, the scientific goals, and the instrumentation is given by Oelhaf et al. (2019).

A summary of the Falcon flight tracks performed during GW-LCYCLE II is shown in Fig. 1. Altogether, 6 research flights with a total of about 20 flight hours were performed. The flights were planned along and across the Scandinavian Alps to
probe the excitation region of mountains waves (MWs). The HALO flight track flown on 28 January 2016 is additionally plotted (yellow line) as it was particularly coordinated with the two Falcon flights performed on that day (dark and light blue lines). The geolocation of Kiruna airport is indicated by the black cross, and the flight leg (FL3), where the novel GW-scan was applied to the 2-μm DWL, is marked by the black dots.

2.2 Coordinated research flights on 28 January 2016

The 28 January 2016 was a favorable day because of several reasons. First, the excitation of MWs was likely due to moderate wind speeds blowing perpendicular to the Scandinavian mountain ridge. Second, the research flights of HALO and Falcon were coordinated, giving the possibility of using additional measurement data for GW characterization. And third, the 2-μm DWL
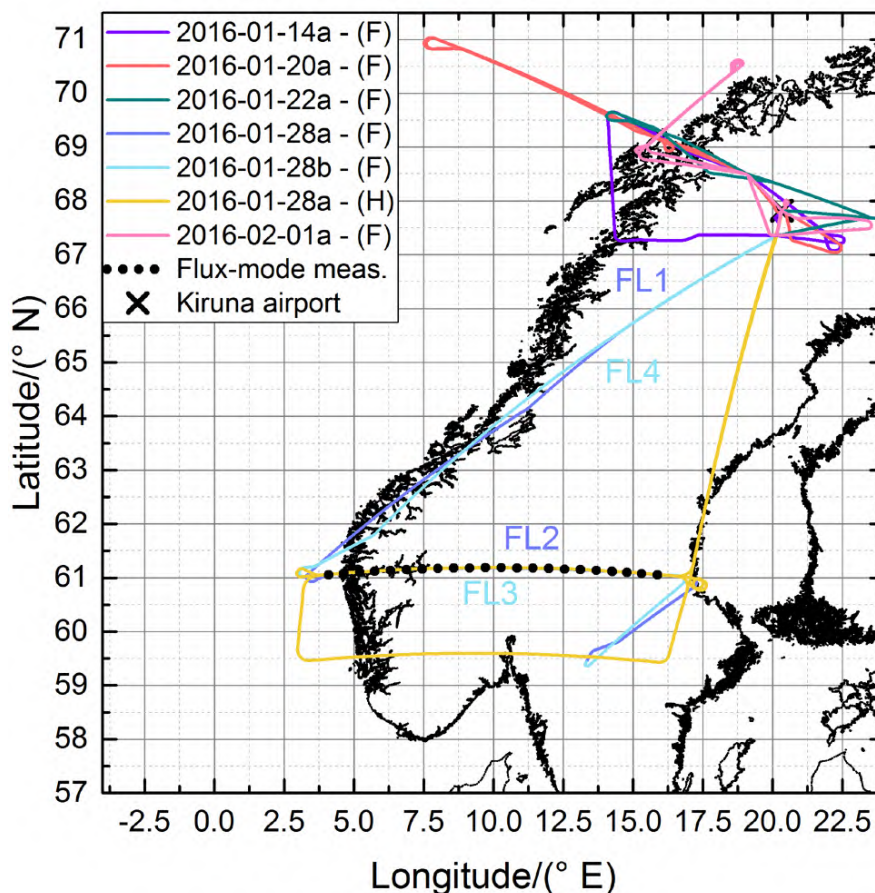
Figure 1. Overview of the Falcon (F) flight tracks flown during GW-LCYCLE II and the coordinated HALO (H) flight track flown on 28 January 2016 (see label). The black dots indicate the region where the new GW mode scan pattern was performed. The black cross denotes the geolocation of Kiruna airport. An overview of the respective 2-μm DWL measurement modes during the flight legs (FL) performed on 28 January 2016 is given in table 1.

was operated with a new momentum flux scanning mode (MF-mode) to measure the vertical and the horizontal wind along the flight track, simultaneously.

90   The meteorological situation on 28 January 2016 was featured by two synoptic low-pressure systems, one over the tip of Greenland and one over the Baltic sea, leading to moderate south-westerly winds of 10 m s^{-1} to 20 m s^{-1} in the troposphere and thus, to the excitation of MWs over the Scandinavian mountain range (Gisinger et al., 2020). For that reason, a coordinated flight of Falcon and HALO was planned and conducted on this day (Fig. 1, in dark and light blue (Falcon) and yellow (HALO)). The Falcon took off from Kiruna airport at 12:45 UTC and climbed to an altitude of about 9.8 km. The first flight leg (Fig. 1,

95   FL1) started in southern direction along the Scandinavian coast with the 2-μm DWL operating in wind-mode, giving the possibility to investigate the inflow conditions based on the measured wind speed and wind direction. At about 61° N, the

Falcon turned eastwards and flew a 700 km long cross-mountain leg (Fig. 1, FL2) before doing a refueling-stopover at Karlstad airport. On this leg, the 2-μm DWL performed in vertical-wind-mode to resolve the small-scale structure of the excited MWs with a horizontal resolution of about 200 m (see also Sect. 3.2). At 17:10, the Falcon lifted off again and flew the similar
100 flight track back. On the cross-mountain leg (Fig. 1, FL3), the 2-μm DWL was operated in MF-mode to determine the leg-averaged momentum flux profile. At about 61° N, the Falcon turned northwards and flew back to Kiruna airport (Fig. 1, FL4), while measuring with the 2-μm DWL in wind mode again to verify if the inflow conditions have changed since the first flight, which was performed about 4 hours earlier. An overview of the four different flight legs is given in table 1. The respective characteristics of the 2-μm DWL measurement modes, namely wind-mode, vertical-wind-mode, and MF-mode, are presented
105 in Sect. 3.2.

Table 1. Overview Falcon flight legs performed on 28 January 2016 including corresponding 2-μm DWL measurement modes and data productions

Nr.	Flight	Time/(UTC)[*]	Lat./(° N)[*]	Lon./(° E)[*]	Length/(km)	2-μm DWL mode	data product
FL1	20160128a	12:56/14:27	67.19/61.21	19.57/3.65	1019	Wind-mode	Wind vector
FL2	20160128a	14:33/15:23	61.02/61.02	3.89/16.76	703	Vertical-wind-mode	Vertical wind speed
FL3	20160128b	17:38/18:46	61.04/61.02	16.23/3.23	713	MF-mode	Vert./Hor. wind[†]
FL4	20160128b	18:48/20:02	61.17/66.94	3.14/18.73	1002	Wind-mode	Wind vector

[*] Values are start/stop values of the corresponding flight leg (LAT = latitude, LON = longitude).

[†] Horizontal wind is measured along the flight direction (u_{par}).

HALO left Kiruna airport at 16:16 UTC and thus a little later than originally planned due to a technical problem with one of the instruments aboard. Still, it was possible to perform coordinated measurements with the Falcon aircraft. In particular, while the Falcon was flying the cross-mountain leg FL3 at an altitude of 9.8 km, HALO flew below at an altitude of 7.8 km. The horizontal distance between both aircraft was less than 100 m, and the temporal distance was varying between 1 and 2 minutes.
110 Hence, the HALO in-situ measurements of wind speed and direction represent a perfect validation data set for the MF-mode measurements and the corresponding wind retrieval as discussed in Section 3.3 and Section 4.2.

3 The 2-μm Doppler Wind Lidar at DLR

The DLR 2-μm DWL has been deployed in several airborne campaigns within the last two decades to measure for instance the optical properties of aerosols (Chouza et al., 2015, 2017) and horizontal wind speeds over the Atlantic Ocean as input data
115 for numerical weather prediction assimilation experiments (Weissmann et al., 2005; Schäfler et al., 2018). Furthermore, it was extensively used for pre-launch (Marksteiner et al., 2018; Lux et al., 2018) and post-launch validation activities of the first space-borne wind lidar Aeolus (Witschas et al., 2020; Lux et al., 2020; Witschas et al., 2022; Lux et al., 2022). Additionally, horizontal and vertical wind speed measurements have been performed and have been used to characterize the spectral features of orographically induced gravity waves (Witschas et al., 2017; Wagner et al., 2017; Gisinger et al., 2020).

120   In this section, the 2-μm DWL instrumental setup is shortly described (section 3.1), followed by an explanation of the corresponding measurement principle and the applied scanning modes given in section 3.2. Afterward, the data processing steps are discussed in section 3.3, concentrating on the novel momentum flux retrieval. Details about the retrieval procedures of the vertical as well as the horizontal wind speed and direction are given by Witschas et al. (2017).

3.1   Instrumental description

A picture of the 2-μm DWL mounted within the Falcon aircraft is shown in Fig. 2. The 2-μm DWL is a heterodyne-detection
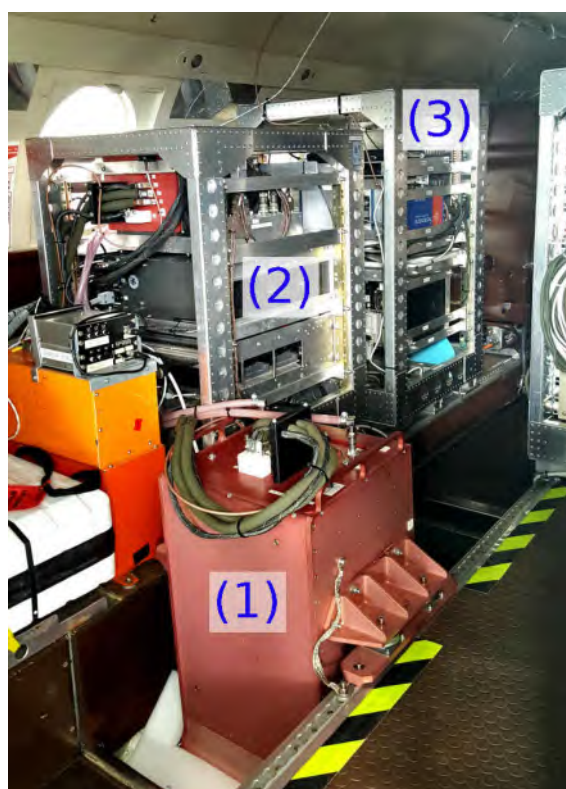
Figure 2. Picture of the 2-μm DWL mounted within the Falcon aircraft showing the transceiver unit (1), the power supply and cooling rack (2) as well as the data acquisition rack (3).

125

wind lidar composed of several sub-units. The heart of the system is the transceiver unit which consists of the laser transmitter, an 11 cm diameter afocal telescope, receiver optics, and a double wedge scanner (Fig. 2, (1)). The transceiver unit (excluding the scanner unit) was built by CLR Photonics (Henderson et al., 1991, 1993; Hannon and Henderson, 1995) and delivered to DLR in 1999. The double-wedge scanner and the data acquisition unit were developed and constructed by DLR (Witschas

130   et al., 2017). The power supply and cooling unit of the system are mounted in a rack located beside the transceiver (Fig. 2, (2)). The corresponding control electronics and the data acquisition unit are mounted in a second rack (Fig. 2, (3)).

The 2-μm DWL system is based on a Tm:LuAG laser producing laser pulses with a wavelength of 2022.54 nm (vacuum), 1 mJ to 2 mJ energy, and a repetition rate of 500 Hz, ensuring eye-safe operation. Before being sent to the atmosphere, the laser beam is expanded by the afocal telescope to a diameter of ≈ 10 mm. The small portion of the light that is scattered back to the instrument is collected with the same telescope and afterward directed to the signal detector, where it is mixed with a local oscillator laser that is also used for injection seeding of the outgoing laser pulse. The time-resolved detector signal resulting from each single laser shot is sampled with 500 MHz and 8 bit resolution. The availability of the signal on a single-shot basis gives maximum flexibility for post-processing (see also section 3.3).

3.2 Measurement principle

Commonly, the 2-μm DWL is used to either measure the three-dimensional wind vector (wind-mode) or rather to measure the vertical wind speed (vertical-wind-mode). When operating in wind-mode, the velocity-azimuth display (VAD) scan technique is applied (Browning and Wexler, 1968) by performing a conical scan around the vertical axis with an off-nadir angle of 20°. Typically, one scanner revolution with 21 line-of-sight (LOS) measurements separated by 18° in the azimuth direction takes about 42 s. By further considering the aircraft speed of about 200 m s^{-1}, the horizontal resolution of 2-μm DWL wind-mode observations is about 8.4 km, depending on the actual ground speed of the aircraft. The vertical resolution is set by the spatial averaging interval to be 100 m considering the full width at half maximum of the laser pulse of ≈ 400 ns.

When measuring in vertical-wind-mode, the laser beam is pointed to nadir-direction, and thus the measured LOS wind equals the vertical wind speed. To avoid an additional contribution of the horizontal wind speed, the aircraft attitude and potential variations during flight (pitch and roll) are compensated by a scanner control loop on a 1-second basis. As one LOS measurement is averaged over 1 s (500 laser pulses), the horizontal resolution of the vertical wind speed data is about 200 m and the vertical resolution is 100 m as for the wind mode measurements.

Based on GW-LCYCLE I 2-μm DWL data, it was revealed that both wind-mode and vertical-wind-mode profiles are beneficial for characterizing the spectral properties of GWs and their evolution while they are propagating (Witschas et al., 2017). However, it was also discussed that simultaneous measurements of the horizontal and the vertical wind speed would be even more beneficial as such measurements would allow retrieving the vertical flux of horizontal momentum induced by GWs (Smith et al., 2008, 2016). To cope with that issue, a new scan pattern with alternately fore and aft propagating laser beams (MF-mode) was applied to the 2-μm DWL for the first time during the GW-LCYCLE II campaign (see also Sect. 3.3 and Fig. 3). A similar approach was already introduced by Vincent and Reid (1983) using a ground-based Doppler radar. Here, this approach is adapted to airborne wind lidar measurements which further enable spatial discrimination compared to the ground-based radar measurements. Considering that the wind field is constant for the time of intersecting fore and aft laser beam pairs, and flying along wind direction, this scan pattern gives the possibility to retrieve vertical wind speed and the horizontal wind component along the flight direction, simultaneously. To assure reasonable data coverage even in clear air conditions, each pointing direction was kept for 2 s. Thus, the retrieved MF-scan data (u_{par} and w) has a horizontal resolution of ≈ 800 m and a vertical resolution of 100 m, which is high enough to resolve even small-scale MWs with horizontal wavelengths of 1.6 km and larger.

3.3 Data processing

When operating in MF-mode, the 2-μm DWL scanner steers the laser beam alternately fore (Fig. 3, blue) and aft (Fig. 3, green) with a certain off-nadir angle θ (usually $20°$) as illustrated in Fig. 3. This procedure results in LOS wind measurements in forward direction v_{f_i} and in backward direction v_{b_i} according to

$$v_{f_i}(R, \theta_{f_i}, x) = w(R, \theta_{f_i}, x)\cos(\theta_{f_i}) + u_{par}(R, \theta_{f_i}, x)\sin(\theta_{f_i})$$
$$v_{b_i}(R, \theta_{b_i}, x) = w(R, \theta_{b_i}, x)\cos(\theta_{b_i}) + u_{par}(R, \theta_{b_i}, x)\sin(\theta_{b_i}) \tag{1}$$

where θ_{f_i} and θ_{b_i} are the actual off-nadir angles of the forward and backward directed laser beam, respectively, x denotes the horizontal distance and R the vertical distance from the aircraft. As the laser beam pointing direction and thus the off-nadir angles are accurately known from the scanner position and the aircraft attitude measured by an inertial reference system (IRS), the two remaining unknowns, namely the horizontal wind speed along flight direction u_{par} and the vertical wind speed w, can directly be derived from a successive pair of v_{f_i}, v_{b_i} measurements according to

$$u_{par}(x, R) = \csc(\theta_{f_i} + \theta_{b_i})(-v_{b_i}\cos\theta_{f_i} + v_{f_i}\sin\theta_{b_i})$$
$$w(x, R) = \csc(\theta_{f_i} + \theta_{b_i})(v_{b_i}\sin\theta_{f_i} + v_{f_i}\cos\theta_{b_i}) \tag{2}$$

where $\csc(z) = 1/\sin(z)$ denotes the cosecant function. The beam pairs have to be chosen such that they intersect at the respective horizontal position (x) and vertical position (R) as illustrated in Fig. 3. To obtain a continuous data set for the fore and aft measured LOS velocities (v_f and v_b excluding the white regions indicated in Fig. 3), the data is linear interpolated.

4 Results

In this section, the findings obtained from the 2-μm DWL measurements acquired on 28 January 2016 are discussed. In Sect. 4.1, the results from horizontal and vertical wind observations are shown, revealing the overall inflow conditions as well as pronounced changes of the horizontal scales in the vertical velocity field. In Sect. 4.2, the accuracy and precision of the MF-mode measurements are estimated by utilizing a comparison against HALO in-situ wind measurements. In Sect. 4.3, the characteristics of the derived leg-averaged horizontal momentum flux profile are discussed.

4.1 Horizontal and vertical wind speed

The horizontal wind speed and wind direction measured on leg FL1 and leg FL4 are shown in Fig. 4. It can be seen that the horizontal wind was blowing with up to $35\ \mathrm{m\ s^{-1}}$ at altitudes between $4\ \mathrm{km}$ and $10\ \mathrm{km}$ from westerly directions, and that the largest wind speeds were located between $62°$ N and $63°$ N. As this situation was forecasted well, the cross-mountain leg was flown south of Kiruna ($\approx 61°$ N) to probe the GW excitation region. At this latitude, the wind direction was measured to be between $260°$ N and $300°$ N and thus, almost perpendicular to the Scandinavian mountain ridge and along the Falcon flight track direction. Thus, this situation provided excellent conditions both for the excitation of MWs as well as for the first
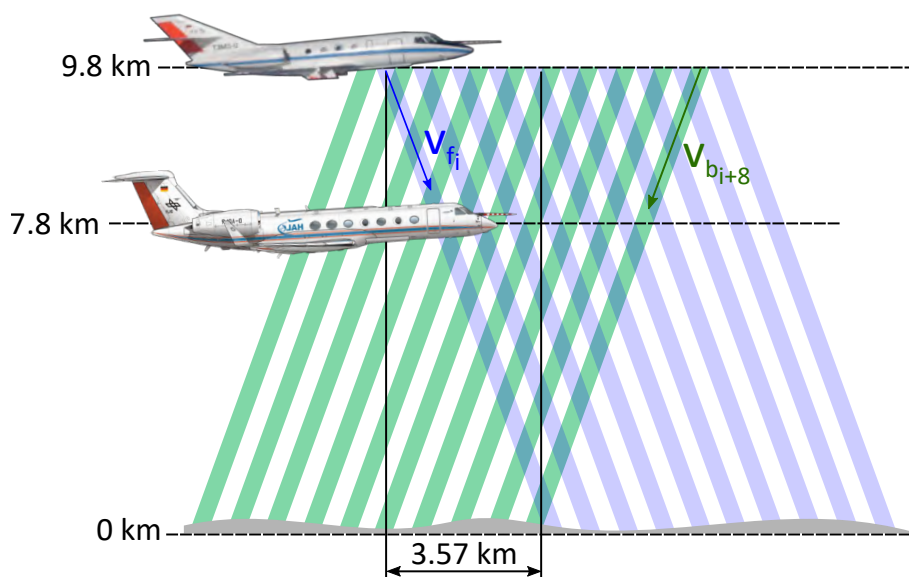
Figure 3. Schematic illustration of the scan procedure applied when operating in MF-mode to retrieve profiles of the horizontal wind along flight direction u_{par} and the vertical wind w, simultaneously.

application of MF-mode, as the corresponding observations only provide the vertical wind speed and the horizontal wind speed along the flight direction (see also section 3.3). By comparing the data from FL1 (Fig.4, left) and FL4 (Fig.4, right), it can be furthermore realized that the horizontal wind speed slightly increased to up to $40 \mathrm{~m~s^{-1}}$, and the location of the local wind
195 speed maximum moved north. Still, the wind direction remained perpendicular to the mountain ridge for all altitudes, which confirms the assumption of steady inflow conditions during the observation period.

At about $61°$ N, the Falcon turned eastward and performed the first cross-mountain leg, while the 2-μm DWL was measuring in vertical-wind-mode. The acquired data is shown in Fig. 5. First, it is obvious that the data coverage of the lidar measurements is sparse, which is on the one hand due to the aerosol-poor atmospheric conditions, and on the other hand due to clouds at the
200 tropopause level and below ($7 \mathrm{~km}$ to $8 \mathrm{~km}$) which prevents the laser beam to propagate to lower altitudes. Still, from the data, it can be seen that MWs are excited. The vertical wind speed along the flight leg varies between $\pm 3 \mathrm{~m~s^{-1}}$. In the western part of the flight leg, the wind speeds are a little lower ($\pm 1 \mathrm{~m~s^{-1}}$) and get larger while going eastward (downstream). Analyzing the spectral structure of the excited GWs, an interesting behavior can be observed between $5°$ E to $8°$ E (see also the light-gray line in Fig. 5). Below altitudes of $\approx 8.5 \mathrm{~km}$, and thus below the thermal tropopause, which is determined using European
205 Centre for Medium-Range Weather Forecasts (ECMWF) model data, the waves have a horizontal wavelength of about $20 \mathrm{~km}$, whereas the ones in or rather above the tropopause have a horizontal wavelength of only $10 \mathrm{~km}$ and smaller. As discussed by Gisinger et al. (2020) based on idealized numerical simulations, this can be explained by the occurrence of interfacial waves in the TIL region. Further eastward ($8°$ E to $16°$ E) only the MWs with the shorter wavelengths ($\lambda < 10 \mathrm{~km}$) are visible as clouds at the tropopause prevented measurements below. At the end of the flight leg ($16°$ E to $17°$ E) the spectral change of
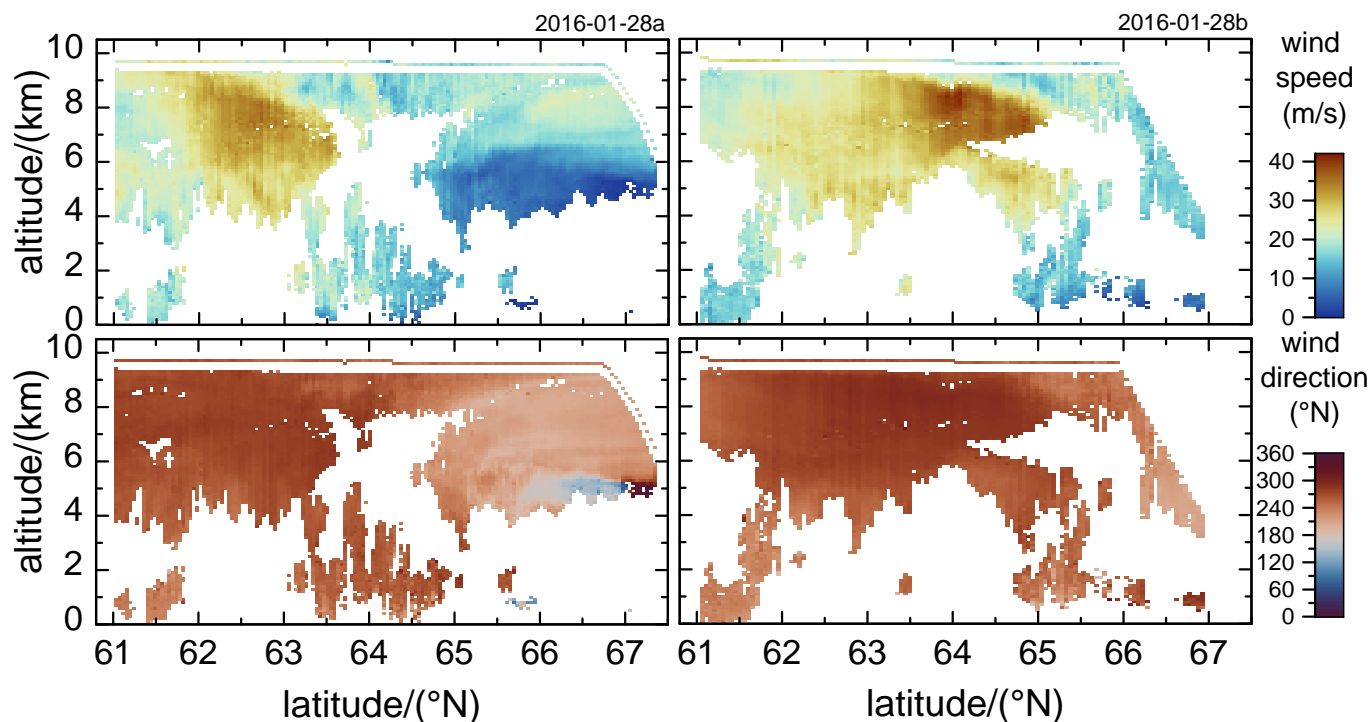
Figure 4. Horizontal wind speed (top) and wind direction (bottom) derived from 2-μm DWL observations acquired in wind-mode on the flight legs FL1 (left) and FL4 (right) flown on 28 January 2016 (see also table 1, and Fig. 1). The corresponding wind speed and direction measured in-situ by the Falcon nose-boom is indicated by the thin line at flight level.

the MWs at the tropopause inversion (at ≈ 8 km altitude) is again obvious. This result demonstrates that the height-resolved vertical-wind-mode data is useful to observe dynamical changes in the wave field with altitude.

4.2 Accuracy of MF-mode measurements

During several campaigns within the last years, the accuracy (systematic error) and the precision (random error) of 2-μm DWL wind-mode and vertical-wind-mode observations were determined utilizing dropsonde comparisons. In particular, the random error of single LOS measurements is characterized to be 0.2 m s^{-1} and the systematic error is smaller than 0.05 m s^{-1} (Witschas et al., 2017). The mean errors for wind-mode observations varies between -0.03 m s^{-1} and 0.08 m s^{-1} (systematic error) and 0.92 m s^{-1} and 1.50 m s^{-1} (random error), whereas these errors contain contributions from both the 2-μm DWL and the dropsonde (Witschas et al., 2020; Weissmann et al., 2005; Chouza et al., 2016; Reitebuch et al., 2017; Schäfler et al., 2018; Witschas et al., 2017).

As the temporal and spatial resolution, as well as the representativity, is different for MF-mode measurements, it was questionable how this affects the systematic and random error of the retrieved wind data. For that reason, HALO in-situ wind data, acquired on the coordinated flight leg with Falcon and HALO on 28 January 2016 (Fig. 1, FL3), are used for validation.
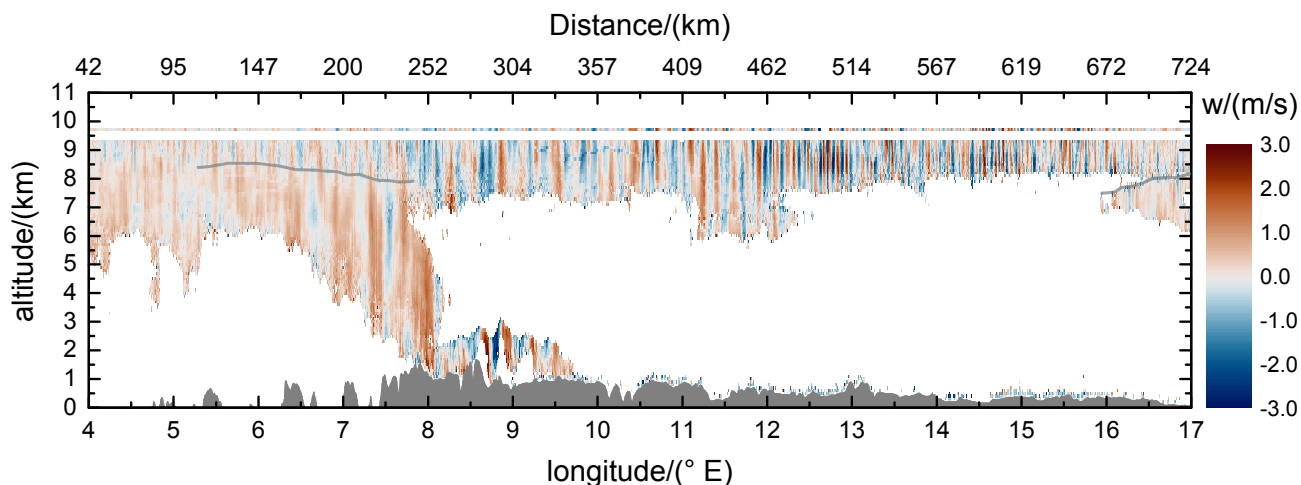
Figure 5. Vertical wind speed derived from 2-μm DWL observations acquired in vertical-wind-mode on the flight leg FL2 flown on 28 January 2016 (see also table 1, and Fig. 1). The corresponding vertical wind measured in-situ by the Falcon nose-boom is indicated by the thin line at flight level. The surface elevation is sketched by the gray area at the bottom of the graph. The light-gray line between 7.5 km and 8.5 km altitude indicates the position of the TIL, where the spectral properties of the GWs change remarkably.

During this flight leg, the Falcon aircraft was flying at 9.8 km altitude, whereas HALO was flying at 7.8 km altitude. The systematic/random errors of HALO in-situ wind measurements are estimated to be $0.4 \text{ m s}^{-1}/0.25 \text{ m s}^{-1}$ for the vertical wind speed and $0.6 \text{ m s}^{-1}/0.3 \text{ m s}^{-1}$ for the horizontal wind speed (Mallaun et al., 2015; Giez et al., 2017, 2021), whereas the similar uncertainty is considered for the horizontal wind along flight direction (u_{par}). The vertical and the horizontal wind speed along flight direction retrieved from the 2-μm DWL data at 7.8 km are shown by the black line in the top-left and top-right panel, respectively. The corresponding data measured in-situ on the HALO aircraft is indicated by the red dashed line. The bottom panels show the corresponding residuals. It can be seen that both measurements are in great accordance along the entire flight leg with its length of almost 700 km. The mean of the vertical wind speed residual, which is an estimate of the mean systematic error, is 0.01 m s^{-1}, and the corresponding standard deviation is 0.3 m s^{-1}. This demonstrates that the vertical wind speed retrieved from the 2-μm DWL is almost bias-free, and the random error $\sigma_{\text{DWL}_{\text{vert}}}$ is $\approx 0.17 \text{ m s}^{-1}$, considering the specified random error of HALO vertical wind speed measurements of 0.25 m s^{-1} and assuming the errors to be uncorrelated ($\sigma_{\text{DWL}_{\text{vert}}} = ((0.3 \text{ m s}^{-1})^2 - (0.25 \text{ m s}^{-1})^2)^{1/2} = 0.17 \text{ m s}^{-1}$).

For u_{par}, the mean of the residual data is -0.76 m s^{-1} and the corresponding standard deviation is 0.58 m s^{-1}. The slightly larger error is probably due to slightly different heading angles of the two aircraft flying at different altitudes which may lead to uncertainties in the wind projection due to the slightly different wind directions retrieved from the respective measurements. Moreover, the 2-μm DWL data represents the mean wind speed at an altitude of (7.8 ± 0.05) km, whereas the HALO in-situ data represents the wind speed at flight level. Thus, vertical gradients in the horizontal wind field could also lead to the observed difference in u_{par} between 2-μm DWL and HALO data. Still, all GW induced structures are visible in both datasets. And as the momentum flux calculation is based on the perturbations of u_{par}, the enhanced systematic error is negligible in this particular
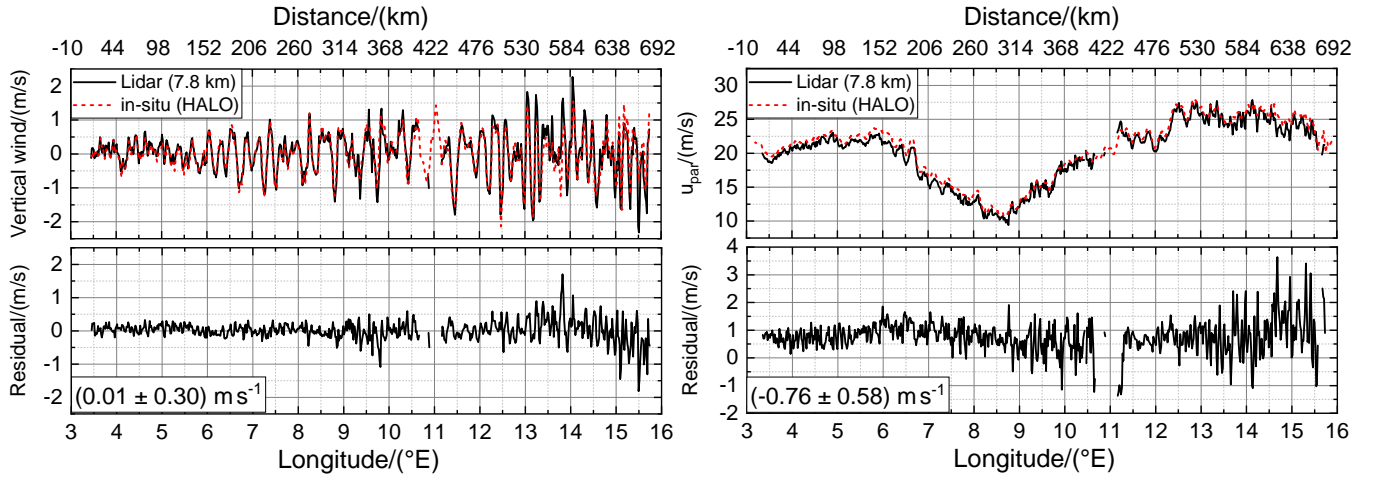
Figure 6. Vertical wind speed (left) and horizontal wind speed along flight direction (right) derived from 2-μm DWL observations acquired in MF-mode on FL3 at 7.8 km altitude (black), and the wind speed measured in-situ at the HALO aircraft flying at the same altitude (red). The bottom panels indicate the corresponding residuals.

case. Considering the random error of 0.3 m s^{-1} specified for HALO horizontal wind speed measurements, the random error $\sigma_{\text{DWL}_{\text{hor}}}$ of u_{par} can be estimated to be 0.5 m s^{-1} or better ($\sigma_{\text{DWL}_{\text{hor}}} = ((0.58 \text{ m s}^{-1})^2 - (0.30 \text{ m s}^{-1})^2)^{1/2} = 0.50 \text{ m s}^{-1}$).

4.3 Momentum flux profile

245 From the simultaneous measurements of u_{par} and w the spatial leg-averaged vertical flux of horizontal momentum MF_{x} can be derived as for instance introduced by Smith et al. (2016) according to

$$\text{MF}_{\text{x}}(z) = \overline{\rho}(z) \frac{1}{L} \cdot \int_0^L u'_{\text{par}}(z) \, w'(z) dx, \tag{3}$$

where $\overline{\rho}$ is the mean air density taken from ECMWF integrated forecast system (IFS) data at respective altitudes, z, and L denotes the length of the flight leg which is usually several hundred kilometers long and thus much longer than the expected

250 GW wavelength. The quantities u'_{par} and w' are the perturbations of the horizontal wind speed along the flight track and the vertical wind speed, respectively, and are derived by subtracting a mean wind profile from the respective measurement data. For the horizontal wind, a 5th-order polynomial fit is applied in a horizontal direction per each range gate altitude and is used for subtraction (Witschas et al., 2017). For the vertical wind, the mean vertical wind along the flight leg $\overline{w}$ is used as background.

The derived horizontal wind along flight direction u_{par}, the corresponding disturbances u'_{par}, the vertical wind speed and

255 $u'_{\text{par}} w'$ measured on FL3 are shown in Fig. 7, (a), (b), (c) and (d), respectively. The horizontal wind speed along the flight track u_{par} (Fig. 7, a) was measured to vary between about 30 m s^{-1} in the eastern part of the flight leg (10° E to 15° E) and about 8 m s^{-1} in the western part (7° E to 10° E), where the change occurs on a wavelength scale of about 400 km, as it
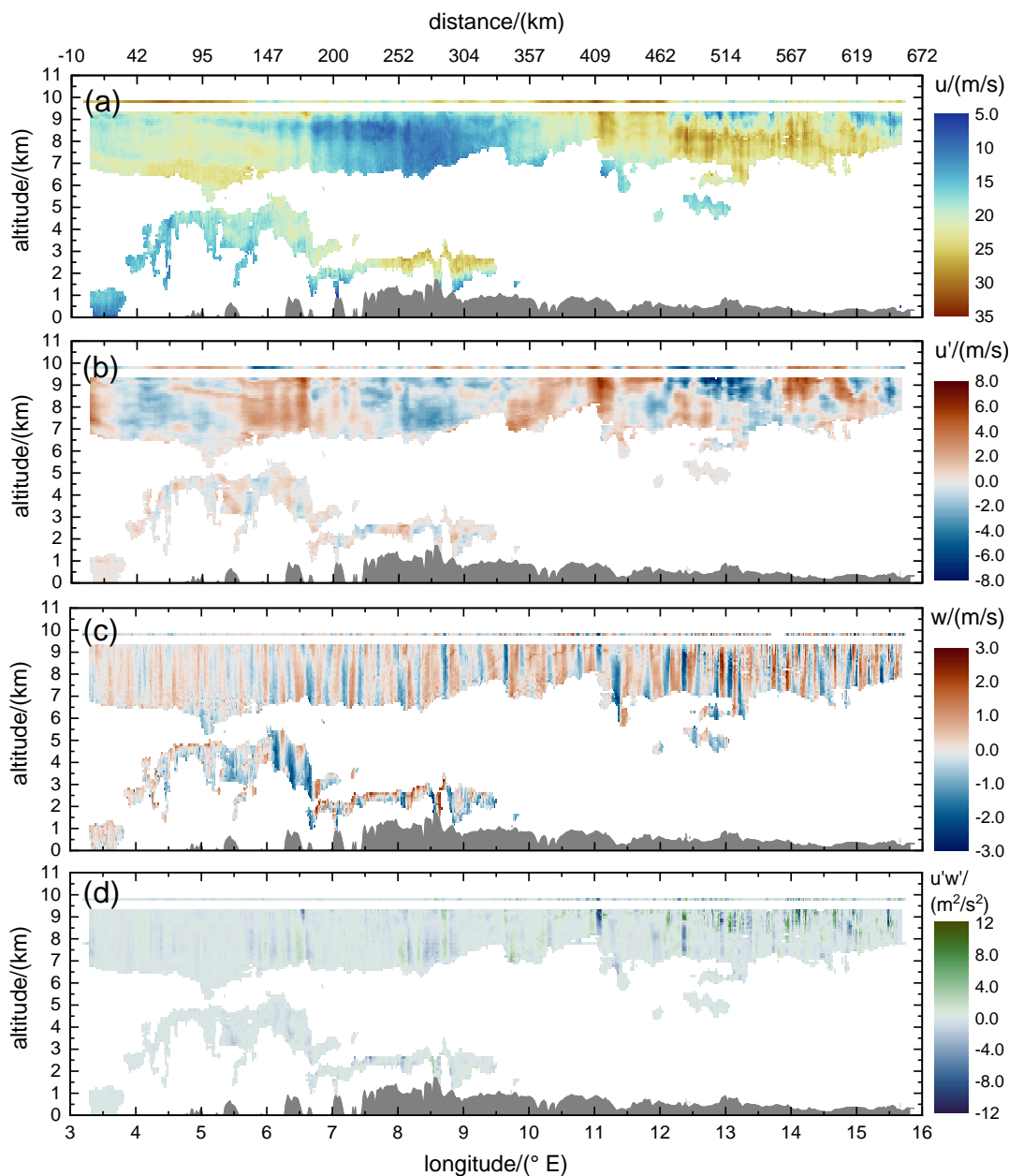
Figure 7. Horizontal wind speed along flight direction u_{par} (a), perturbations of the horizontal wind speed along flight direction u'_{par} (b) and vertical wind speed w (c), as well as $u'_{par} w'$ (d) retrieved from the 2-μm DWL while operating in MF-mode on FL3 performed on 28 January 2016 (see also table 1, and Fig. 1). The thin line at 9.8 km altitude indicates the corresponding wind speed measured in-situ by the nose-boom of the aircraft. The orography is denoted by the gray area.

can also be seen from Fig. 7, b. The disturbances of the horizontal wind speed u'_{par} additionally show features with shorter
wavelengths of about 200 km and an amplitude of $\approx \pm 2 \; \text{m s}^{-1}$. The vertical wind speed (Fig. 7, c) looks comparable to the one

260   measured on FL2 (see also Fig. 5) which further confirms the reliability of MF-mode measurements and stable atmospheric
conditions during the flight period. The vertical wind speed varies between $-3 \; \text{m s}^{-1}$ and $3 \; \text{m s}^{-1}$ and shows horizontal scales
of the order of 10 km. Thus, the observed spectral properties of the observed horizontal and vertical wind speeds are in-line
with what was seen from GW-LCYCLE I data (Witschas et al., 2017) who revealed that the vertical wind speed spectrum
mainly represents the short-wave spectrum of the topography, whereas the spectrum of the horizontal wind speed perturbations

265   is dominated by the long-wave part but additionally shows an influence on the shorter wavelengths. Similar observations have
been made by Smith and Kruse (2017) based on airborne in-situ data. In Fig. 7, d, the derived $u'_{\text{par}} w'$ along the flight leg
is shown. It can be seen that amplitudes of up to $\approx \pm 10 \; \text{m}^2 \; \text{s}^{-2}$ are reached, especially in the downstream region ($12°$ E to
$15.5°$ E).

To further analyze the vertical evolution of the spectral characteristics of $u'_{\text{par}} w'$, wavelet power spectra are calculated in

270   different altitudes as shown in Fig. 8. The left column (a) shows $u'_{\text{par}} w'$ retrieved from the 2-μm DWL measurements at 7.8,
8.2, 8.8, and 9.2 km altitude, as well as the one retrieved from Falcon in-situ measurements at 9.8 km altitude (black line). For
comparison, $u'_{\text{par}} w'$ retrieved from HALO in-situ measurements at 7.8 km altitude is additionally plotted by the red dashed
line. It has to be noted that the y-axes have different scales adapted to the measurement range. The right column (b) indicates
the corresponding wavelet power spectra, calculated by using a Morlet wavelet with a non-dimensional frequency of $\omega_0 = 6$,

275   and the power spectra are normalized such that they represent the squared amplitude of $u'_{\text{par}} w'$ with a potential sinusoidal
variation (Torrence and Compo, 1998). By comparing $u'_{\text{par}} w'$ derived from the 2-μm DWL (black) and HALO (red, dashed) at
7.8 km altitude, it can be realized that they are in great accordance. Only small deviations are obvious between ≈ 14 to $15°$ E.
The amplitudes vary by $\approx \pm 2 \; \text{m}^2 \; \text{s}^{-2}$ with a maximum value of $\approx -4 \; \text{m}^2 \; \text{s}^{-2}$ at $12.5°$ E longitude. The corresponding
wavelet power spectrum indicates horizontal scales varying from about 10 to 20 km all along the flight leg. The $u'_{\text{par}} w'$ and the

280   corresponding wavelet power spectrum at 8.2 km look rather comparable, with an even more pronounced feature at $12.5°$ E.
At 8.8 km, the spectral features of $u'_{\text{par}} w'$ change significantly. Whereas the amplitudes remain well below $\approx \pm 2 \; \text{m}^2 \; \text{s}^{-2}$ in
the upstream region (3 to $11°$ E), they reach values up to $\approx \pm 8 \; \text{m}^2 \; \text{s}^{-2}$ in the downstream region. The corresponding wavelet
power spectrum shows horizontal scales mainly below 10 km, occurring in the downstream region. A similar characteristic
is shown at 9.2 km. At an altitude of 9.8 km (Falcon in-situ data), the amplitudes of $u'_{\text{par}} w'$ decreased to $\approx \pm 4 \; \text{m}^2 \; \text{s}^{-2}$ in

285   the downstream region, and the corresponding wavelet power spectrum is dominated by horizontal wavelengths smaller than
10 km. Thus, this analysis demonstrates that the spectral features of the momentum flux change significantly in the tropopause
region.

From the range-resolved measurements of $u'_{\text{par}} w'$ (Fig. 7, d), the profile of the leg-averaged vertical flux of horizontal
momentum MF_{x} is derived according to Eq. (3) and shown in Fig. 9. As already demonstrated by Brown (1983), it is useful to

290   estimate the uncertainty of the leg-averaged MF_{x} values that is induced by the leg-length itself and a potentially related unequal
sampling of updrafts and downdrafts. To cope with that issue, MF_{x} is calculated for several sub-legs with a fixed start point at
the westernmost point of the track and a varying leg length. The minimum leg length is 200 km and is stepwise increased by
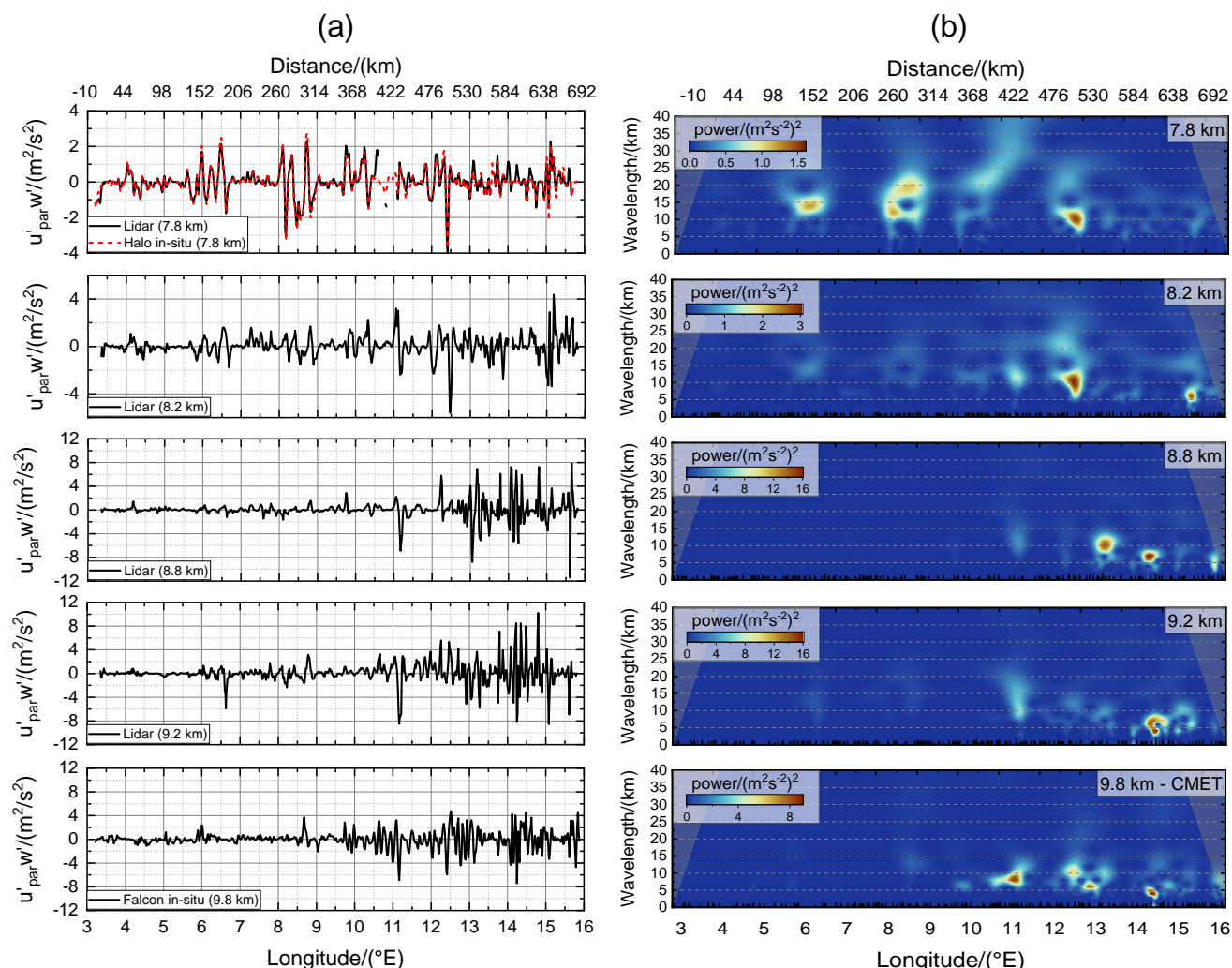
Figure 8. The left column (a) shows $u'_{\mathrm{par}} w'$ retrieved in different altitudes from the 2-μm DWL measurements (7.8, 8.2, 8.8 and 9.2 km) and from Falcon in-situ measurements (9.8 km). For comparison, $u'_{\mathrm{par}} w'$ retrieved from HALO in-situ measurements at 7.8 km is additionally plotted by the red dashed line. The ride side (b) indicates the corresponding wavelet power spectra, calculated by using a Morlet wavelet.

1 km intervals until the maximum leg length of 700 km is reached. The same procedure is additionally applied starting from the easternmost point of the flight track. Afterward, the mean and standard deviation for all sub-legs is calculated, whereas the

295   determined standard deviation represents the sensitivity of the leg-averaged $\mathrm{MF_x}$ to the start/end points and the length of the flight leg.

In Fig. 9, the $\mathrm{MF_x}$ retrieved from the 2-μm DWL is indicated by the black line and the corresponding uncertainty is indicated by the gray area. The respective $\mathrm{MF_x}$ values obtained from Falcon and HALO in-situ data are denoted by the red and blue dots, respectively. It can be seen that 2-μm DWL and HALO in-situ data at 7.8 km altitude differs significantly which is surprising,

300 as almost no differences can be observed from the respective measurements of u_{par} and w (see also Fig. 6 and Fig. 8, a, top). However, both measurements still compare within their uncertainties (Fig. 9, blue error bars, and gray area), which also confirms that the sub-leg averaging procedure described before is a good method for estimating the $\mathrm{MF_x}$ uncertainty.

It is worth mentioning, that the presented method to derive the zonal momentum flux only works reliably in the case of having unidirectional flow conditions along the entire flight leg, as only the wind component along the flight track is measured. For the

305 shown example case, it was verified using ECMWF-IFS data, that u_{par} deviated from the horizontal wind speed by a maximum of $\pm 2~\mathrm{m~s^{-1}}$ in the analyzed altitude range (7.8 to 9.8 km), and thus, by less than 10%. Furthermore, the uncertainty induced by these slight changes, caused by a small wind direction change along the flight leg in different altitudes, is partly considered by the sequential leg integration as discussed before. To derive a reliable profile of the total momentum flux, a modified scan pattern with fore/aft and additionally left/right steering laser beams is foreseen for future applications, to measure both, the

310 horizontal wind component parallel to the flight direction u_{par} as well as perpendicular to the flight direction u_{per}.

The derived flux profile exhibits prominent features. Below 8 km, $\mathrm{MF_x}$ is negative, indicating an upward propagation, whereas $\mathrm{MF_x}$ is positive between 8.0 km and 9.3 km around the tropopause, suggesting downward propagation. This points to a reflection or rather trapping of the MWs in the vicinity of the TIL region. The $\mathrm{MF_x}$ at 7.8 km altitude of the 2-μm DWL and the HALO in-situ data differs but within the range of the uncertainty. It also can be seen that the uncertainty in the $\mathrm{MF_x}$

315 from the in-situ data is larger than the uncertainty derived for the 2-μm DWL data. The largest $\mathrm{MF_x}$ values of ≈ 0.06 Pa are found at an altitude of 8.3 km which can be explained by the occurrence of interfacial waves in the TIL region (Gisinger et al., 2020). This exampled demonstrates, that the new 2-μm DWL MF-mode measurements extend the possibilities to characterize the properties of orographically induced GWs.

5 Summary

320 In the framework of the GW-LCYCLE II campaign, which took place from 12 January 2016 to 3 February 2016 in northern Scandinavia, the DLR 2-μm DWL was deployed on the DLR Falcon research aircraft and was, together with other airborne and ground-based instruments, used to investigate the properties of orographically induced GWs over the Scandinavian mountain ridge. To extend the capabilities of the 2-μm DWL to measure the vertical wind and the horizontal wind along flight direction simultaneously, a novel momentum flux scanning mode (MF-mode), with alternately fore and aft propagating laser beams

325 was applied on a cross-mountain flight leg performed on the second research flight on 28 January 2016. As this flight leg was coordinated with the HALO aircraft flying at lower altitudes of 7.8 km, HALO in-situ measurements could be used to validate the functionality of MF-mode measurements and the corresponding retrieval algorithms. It is shown that the derived vertical wind speeds have a mean systematic error of only $0.01~\mathrm{m~s^{-1}}$ and a corresponding random error of $0.17~\mathrm{m~s^{-1}}$. For the horizontal wind speed measured along flight direction, the systematic error is $0.76~\mathrm{m~s^{-1}}$ and the random error is $0.50~\mathrm{m~s^{-1}}$,

330 whereas the systematic error is composed of the 2-μm DWL contribution and the one of the HALO measurements which is specified to be $\approx 0.6~\mathrm{m~s^{-1}}$.
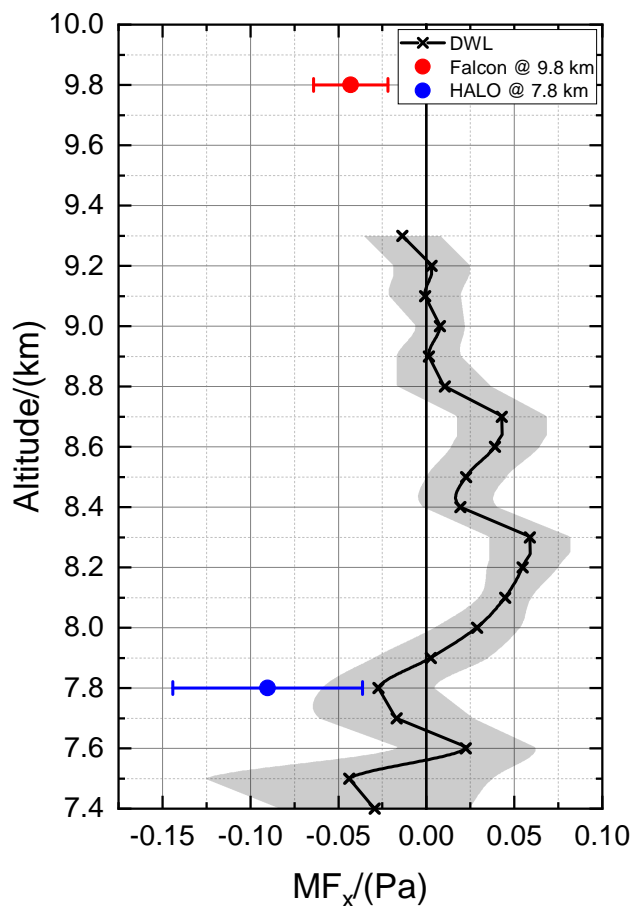
Figure 9. Leg-averaged momentum flux profile calculated according to Eq. (3) as mean for varying leg length (solid) with standard deviation (shading, error bars) for the 2-μm DWL ($\times$) and the in-situ measurements ($\bullet$).

Horizontal wind speed measurements performed by the 2-μm DWL along the Scandinavian coast are shown to be useful to characterize the overall inflow conditions. They revealed that the wind was blowing with up to $30\,\mathrm{m\,s^{-1}}$ in the region where the Falcon cross-mountain leg was performed ($\approx 61°$ N) and that wind direction was more or less perpendicular to the orientation

335   of the mountain ridge in all altitudes (from the ground up to $9.8\,\mathrm{km}$).

Vertical wind speed measurements with a higher horizontal resolution of about $200\,\mathrm{m}$ clearly show the excitation of GWs. The amplitudes of the vertical wind speed reach values of up to $\pm 3\,\mathrm{m\,s^{-1}}$. Furthermore, a change in the horizontal wavelength is observed in the downwind region ($5°$ N to $8°$ N) and altitudes of about $8\,\mathrm{km}$. As discussed by Gisinger et al. (2020), this behavior could be explained by the occurrence of interfacial waves in the TIL region that was existing during this event and

340   that extended to these altitudes.

Based on MF-mode data, the leg-averaged horizontal momentum profile was derived. Negative fluxes of $0.025 \ \mathrm{m^2 \ s^{-2}}$ were determined at an altitude of 8 km, indicating an upward propagation. On contrary, $\mathrm{MF_x}$ was positive above 8 km up to 9.3 km, suggesting a downward propagation, which points to a reflection or trapping of MWs in the tropopause region.

Hence, this analysis demonstrates that 2-μm DWL measurements, in general, are beneficial compared to in-situ measure-
345   ments as they provide similar accuracy and a sufficient horizontal resolution, but wind information in several altitudes enables to study the GW propagation processes more accurately. The MF-mode measurements are particularly useful, as they further allow to characterize the momentum flux profile and with that, to gain knowledge about the propagation direction of the excited GWs. An adaption of the presented MF-mode measurements by the observation of the horizontal wind component perpendicular to the flight direction (u_{per}) is foreseen for future applications to be able to derive the total momentum flux
350   profile.

Author contributions. Benjamin Witschas prepared the main part of the paper manuscript, developed the retrieval for the momentum flux from 2-μm DWL data, and performed the corresponding analysis. Stephan Rahm performed the 2-μm DWL data processing and provided the line-of-sight wind speeds and lidar housekeeping data enabling to perform of the momentum flux retrieval. Sonja Gisinger provided an overview of the meteorological conditions during the entire campaign period and contributed to discussions about the physical interpretation
355   of the retrieved momentum flux profiles. Markus Rapp was the principal investigator of the GW-LCYCLE II campaign and contributed to the preparation of the manuscript. Andreas Dörnbrack and Dave Fritts supported the development of the novel GW-scan pattern and contributed to the preparation of the paper manuscript.

Competing interests. The authors declare that they have no conflict of interest.

Acknowledgements. The technical assistance by Engelbert Nagel as well as the support of the DLR flight facility for the realization of the
360   performed validation campaigns is highly acknowledged.

References

Baumgarten, G.: Doppler Rayleigh/Mie/Raman lidar for wind and temperature measurements in the middle atmosphere up to 80 km, Atmospheric Measurement Techniques, 3, 1509–1518, https://doi.org/10.5194/amt-3-1509-2010, 2010.

Bögel, W. and Baumann, R.: Test and calibration of the DLR Falcon wind measuring system by maneuvers, Journal of Atmospheric and Oceanic Technology, 8, 5–18, 1991.

Brown, P. R.: Aircraft measurements of mountain waves and their associated momentum flux over the British Isles, Quarterly Journal of the Royal Meteorological Society, 109, 849–865, 1983.

Browning, K. and Wexler, R.: The determination of kinematic properties of a wind field using Doppler radar, J. Appl. Meteorol., 7, 105–113, https://doi.org/10.1175/1520-0450(1968)007<0105:tdokpo>2.0.co;2, 1968.

Chen, C.-C., Hakim, G. J., and Durran, D. R.: Transient mountain waves and their interaction with large scales, Journal of the Atmospheric Sciences, 64, 2378–2400, https://doi.org/10.1175/jas3972.1, 2007.

Chouza, F., Reitebuch, O., Groß, S., Rahm, S., Freudenthaler, V., Toledano, C., and Weinzierl, B.: Retrieval of aerosol backscatter and extinction from airborne coherent Doppler wind lidar measurements, Atmospheric Measurement Techniques, 8, 2909–2926, https://doi.org/10.5194/amtd-8-1935-2015, 2015.

Chouza, F., Reitebuch, O., Jähn, M., Rahm, S., and Weinzierl, B.: Vertical wind retrieved by airborne lidar and analysis of island induced gravity waves in combination with numerical models and in situ particle measurements, Atmospheric Chemistry and Physics, 16, 4675–4692, https://doi.org/10.5194/acp-2015-1014, 2016.

Chouza, F., Witschas, B., and Reitebuch, O.: Heterodyne high-spectral-resolution lidar, Applied optics, 56, 8121–8134, 2017.

Dörnbrack, A., Leutbecher, M., Reichardt, J., Behrendt, A., Muller, K.-P., and Baumgarten, G.: Relevance of mountain wave cooling for the formation of polar stratospheric clouds over Scandinavia- Mesoscale dynamics and observations for January 1997, Journal of Geophysical Research, 106, 1569–1581, https://doi.org/10.1029/2000jd900194, 2001.

Ehard, B., Achtert, P., Dörnbrack, A., Gisinger, S., Gumbel, J., Khaplanov, M., Rapp, M., and Wagner, J.: Combination of lidar and model data for studying deep gravity wave propagation, Monthly Weather Review, 144, 77–98, 2016a.

Ehard, B., Achtert, P., Dörnbrack, A., Gisinger, S., Gumbel, J., Khaplanov, M., Rapp, M., and Wagner, J.: Combination of lidar and model data for studying deep gravity wave propagation, Monthly Weather Review, 144, 77–98, 2016b.

Eliassen, A. and Palm, E.: On the transfer of energy in stationary mountain waves, Geofysiske Publikasjoner, 22, 1–23, 1961.

Fritts, D. C. and Alexander, M. J.: Gravity wave dynamics and effects in the middle atmosphere, Reviews of Geophysics, 41, https://doi.org/10.1029/2001RG000106, 2003.

Fritts, D. C., Smith, R. B., Taylor, M. J., Doyle, J. D., Eckermann, S. D., Dörnbrack, A., Rapp, M., Williams, B. P., Pautet, P.-D., Bossert, K., Criddle, N. R., Reynolds, C. A., Reinecke, P. A., Uddstrom, M., Revell, M. J., Turner, R., Kaifler, B., Wagner, J. S., Mixa, T., Kruse, C. G., Nugent, A. D., Watson, C. D., Gisinger, S., Smith, S. M., Lieberman, R. S., Laughman, B., Moore, J. J., Brown, W. O., Haggerty, J. A., Rockwell, A., Stossmeister, G. J., Williams, S. F., Hernandez, G., Murphy, D. J., Klekociuk, A. R., Reid, I. M., and Ma, J.: The Deep Propagating Gravity Wave Experiment (DEEPWAVE): An Airborne and Ground-Based Exploration of Gravity Wave Propagation and Effects from Their Sources throughout the Lower and Middle Atmosphere, Bulletin of the American Meteorological Society, 97, 425–453, https://doi.org/10.1175/BAMS-D-14-00269.1, 2016.

Giez, A., Mallaun, C., Zöger, M., Dörnbrack, A., and Schumann, U.: Static pressure from aircraft trailing-cone measurements and numerical weather-prediction analysis, Journal of Aircraft, 54, 1728–1737, 2017.

Giez, A., Mallaun, C., Nenakhov, V., and Zöger, M.: Calibration of a Nose Boom Mounted Airflow Sensor on an Atmospheric Research
 Aircraft by Inflight Maneuvers, Tech. Rep. No. 2021-17, DLR, Oberpfaffenhofen, https://elib.dlr.de/145704/, 2021.

400 Gisinger, S., Wagner, J., and Witschas, B.: Airborne measurements and large-eddy simulations of small-scale gravity waves at the tropopause
 inversion layer over Scandinavia, Atmospheric Chemistry and Physics, 20, 10 091–10 109, 2020.

Grubišić, V., Doyle, J. D., Kuettner, J., Mobbs, S., Smith, R. B., Whiteman, C. D., Dirks, R., Czyzyk, S., Cohn, S. A., Vosper, S., Weissmann,
 M., Haimov, S., Wekker, S. F. J. D., Pan, L. L., and Chow, F. K.: THE TERRAIN-INDUCED ROTOR EXPERIMENT: A Field Campaign
 Overview Including Observational Highlights, Bull. Am. Meteorol. Soc., 89, 1513 – 1534, https://doi.org/10.1175/2008BAMS2487.1,
405 2008.

Hannon, S. M. and Henderson, S. W.: Wind Measurement Applications of Coherent Lidar., The Review of Laser Engineering (Japan), 23,
 124–130, 1995.

Henderson, S. W., Hale, C. P., Magee, J. R., Kavaya, M. J., and Huffaker, A. V.: Eye-safe coherent laser radar system at 2.1 μm using Tm,
 Ho: YAG lasers, Optics Letters, 16, 773–775, 1991.

410 Henderson, S. W., Suni, P. J., Hale, C. P., Hannon, S., Magee, J. R., Bruns, D. L., and Yuen, E. H.: Coherent laser radar at 2 μm using
 solid-state lasers, IEEE Trans. Geosci. Remote Sens., 31, 4–15, 1993.

Kaifler, B. and Kaifler, N.: A Compact Rayleigh Autonomous Lidar (CORAL) for the middle atmosphere, Atmos. Meas. Tech., 14, 1715–
 1732, 2021.

Kaifler, N., Kaifler, B., Dörnbrack, A., Rapp, M., Hormaechea, J. L., and de la Torre, A.: Lidar observations of large-amplitude mountain
415 waves in the stratosphere above Tierra del Fuego, Argentina, Scientific reports, 10, 1–10, 2020.

Kaifler, N., Kaifler, B., Dörnbrack, A., Gisinger, S., Mixa, T., and Rapp, M.: Multi-scale mountain waves observed with the ALIMA li-
 dar during SOUTHTRAC-GW above the southern Andes, in: EGU General Assembly Conference Abstracts, EGU General Assembly
 Conference Abstracts, pp. EGU21–13 504, https://doi.org/10.5194/egusphere-egu21-13504, 2021.

Krautstrunk, M. and Giez, A.: The transition from FALCON to HALO era airborne atmospheric research, in: Atmospheric physics, pp.
420 609–624, Springer, 2012.

Latteck, R., Singer, W., Rapp, M., Renkwitz, T., and Stober, G.: Horizontally resolved structures of radar backscatter from polar mesospheric
 layers, Advances in Radio Science, 10, 285–290, 2012.

Lukianova, R., Kozlovsky, A., and Lester, M.: Climatology and inter-annual variability of the polar mesospheric winds inferred from meteor
 radar observations over Sodankylä (67°N, 26°E) during solar cycle 24, Journal of Atmospheric and Solar-Terrestrial Physics, 171, 241 –
425 249, https://doi.org/https://doi.org/10.1016/j.jastp.2017.06.005, vertical Coupling in the Atmosphere-Ionosphere System: Recent Progress,
 2018.

Lux, O., Lemmerz, C., Weiler, F., Marksteiner, U., Witschas, B., Rahm, S., Schäfler, A., and Reitebuch, O.: Airborne wind lidar observations
 over the North Atlantic in 2016 for the pre-launch validation of the satellite mission Aeolus, Atmos. Meas. Tech., 11, 3297–3322, 2018.

Lux, O., Lemmerz, C., Weiler, F., Marksteiner, U., Witschas, B., Rahm, S., Geiß, A., and Reitebuch, O.: Intercomparison of wind observations
430 from the European Space Agency's Aeolus satellite mission and the ALADIN Airborne Demonstrator, Atmos. Meas. Tech., 13, 2075–
 2097, 2020.

Lux, O., Lemmerz, C., Weiler, F., Marksteiner, U., Witschas, B., Rahm, S., Geiß, A., Schäfler, A., and Reitebuch, O.: Retrieval improve-
 ments for the ALADIN Airborne Demonstrator in support of the Aeolus wind product validation, Atmos Meas Tech, 15, 1303–1331,
 https://doi.org/10.5194/amt-15-1303-2022, 2022.

435 Mallaun, C., Giez, A., and Baumann, R.: Calibration of 3-D wind measurements on a single-engine research aircraft, Atmospheric Measurement Techniques, 8, 3177–3196, 2015.

Marksteiner, U., Lemmerz, C., Lux, O., Rahm, S., Schäfler, A., Witschas, B., and Reitebuch, O.: Calibrations and Wind Observations of an Airborne Direct-Detection Wind LiDAR Supporting ESA's Aeolus Mission, Remote Sensing, 10, 2056, 2018.

Oelhaf, H., Sinnhuber, B.-M., Woiwode, W., Bönisch, H., Bozem, H., Engel, A., Fix, A., Friedl-Vallon, F., Grooß, J.-U., Hoor, P., et al.:
440 POLSTRACC: airborne experiment for studying the polar stratosphere in a changing climate with the high-altitude long-range research aircraft HALO, Bulletin of the American Meteorological Society, 2019.

Pautet, P.-D., Taylor, M. J., Pendleton, W. R., Zhao, Y., Yuan, T., Esplin, R., and McLain, D.: Advanced mesospheric temperature mapper for high-latitude airglow studies, Appl. Opt., 53, 5934–5943, https://doi.org/10.1364/AO.53.005934, 2014.

Rapp, M., Kaifler, B., Dörnbrack, A., Gisinger, S., Mixa, T., Reichert, R., Kaifler, N., Knobloch, S., Eckert, R., Wildmann, N., Giez, A.,
445 Krasauskas, L., Preusse, P., Geldenhuys, M., Riese, M., Woiwode, W., Friedl-Vallon, F., Sinnhuber, B.-M., de la Torre, A., Alexander, P., Hormaechea, J. L., Janches, D., Garhammer, M., Chau, J. L., Conte, J. F., Hoor, P., and Engel, A.: SOUTHTRAC-GW: An airborne field campaign to explore gravity wave dynamics at the world's strongest hotspot, Bulletin of the American Meteorological Society, pp. 1 – 60, https://doi.org/10.1175/BAMS-D-20-0034.1, 2020.

Reichert, R., Kaifler, B., Kaifler, N., Rapp, M., Pautet, P.-D., Taylor, M. J., Kozlovsky, A., Lester, M., and Kivi, R.: Retrieval of intrin-
450 sic mesospheric gravity wave parameters using lidar and airglow temperature and meteor radar wind data, Atmospheric Measurement Techniques, 12, 5997–6015, https://doi.org/10.5194/amt-12-5997-2019, 2019.

Reitebuch, O., Lemmerz, C., Lux, O., Marksteiner, U., Witschas, B., and Neely, R.: WindVal-Joint DLR-ESA-NASA Wind Validation for Aeolus, Final Report Contract No. 4000114053/15/NL/FF/gp, European Space Agency (ESA), Noordwijk, The Netherlands, 2017.

Schäfler, A., Craig, G., Wernli, H., Arbogast, P., Doyle, J. D., McTaggart-Cowan, R., Methven, J., Rivière, G., Ament, F., Boettcher, M., et al.:
455 The North Atlantic Waveguide and Downstream Impact Experiment, Bulletin of the American Meteorological Society, 99, 1607–1637, 2018.

Smith, R. B. and Kruse, C. G.: Broad-Spectrum Mountain Waves, J. Atmospheric Sci., 74, 1381 – 1402, https://doi.org/10.1175/JAS-D-16-0297.1, 2017.

Smith, R. B., Woods, B. K., Jensen, J., Cooper, W. A., Doyle, J. D., Jiang, Q., and Grubišić, V.: Mountain waves entering the stratosphere, J.
460 Atmospheric Sci., 65, 2543–2562, 2008.

Smith, R. B., Nugent, A. D., Kruse, C. G., Fritts, D. C., Doyle, J. D., Eckermann, S. D., Taylor, M. J., Dörnbrack, A., Uddstrom, M., Cooper, W., et al.: Stratospheric gravity wave fluxes and scales during DEEPWAVE, Journal of the Atmospheric Sciences, 73, 2851–2869, 2016.

Stober, G., Latteck, R., Rapp, M., Singer, W., and Zecha, M.: MAARSY–the new MST radar on Andøya: first results of spaced antenna and Doppler measurements of atmospheric winds in the troposphere and mesosphere using a partial array, Adv, Radio Sci, 10, 291–298, 2012.
465 Torrence, C. and Compo, G. P.: A practical guide to wavelet analysis, Bulletin of the American Meteorological Society, 79, 61–78, 1998.

Vincent, R. and Reid, I.: HF Doppler measurements of mesospheric gravity wave momentum fluxes, Journal of the Atmospheric Sciences, 40, 1321–1333, 1983.

Wagner, J., Dörnbrack, A., Rapp, M., Gisinger, S., Ehard, B., Bramberger, M., Witschas, B., Chouza, F., Rahm, S., Mallaun, C., Baumgarten, G., and Hoor, P.: Observed versus simulated mountain waves over Scandinavia – improvement of vertical winds, energy and momentum
470 fluxes by enhanced model resolution?, Atmos. Chem. Phys., 17, 4031–4052, https://doi.org/10.5194/acp-17-4031-2017, 2017.

Weissmann, M., Busen, R., Dörnbrack, A., Rahm, S., and Reitebuch, O.: Targeted observations with an airborne wind lidar, Journal of Atmospheric and Oceanic Technology, 22, 1706–1719, 2005.

Witschas, B., Rahm, S., Dörnbrack, A., Wagner, J., and Rapp, M.: Airborne wind lidar measurements of vertical and horizontal winds for the investigation of orographically induced gravity waves, Journal of Atmospheric and Oceanic Technology, 34, 1371–1386, 2017.

475 Witschas, B., Lemmerz, C., Geiß, A., Lux, O., Marksteiner, U., Rahm, S., Reitebuch, O., and Weiler, F.: First validation of Aeolus wind observations by airborne Doppler wind lidar measurements, Atmospheric Measurement Techniques, 13, 2381–2396, https://doi.org/10.5194/amt-13-2381-2020, 2020.

Witschas, B., Lemmerz, C., Geiß, A., Lux, O., Marksteiner, U., Rahm, S., Reitebuch, O., and Weiler, F.: Validation of the Aeolus L2B wind product with airborne wind lidar measurements in the polar North Atlantic region and in the tropics, AMTD, 2022.

480 Wüst, S., Schmidt, C., Hannawald, P., Bittner, M., Mlynczak, M. G., and Russell III, J. M.: Observations of OH airglow from ground, aircraft, and satellite: investigation of wave-like structures before a minor stratospheric warming, Atmos. Chem. Phys., 19, 6401–6418, https://doi.org/10.5194/acp-19-6401-2019, 2019.